Supporting Information

Tensile strain-driven interstitial Ru doping structure on the FeCoP/FF electrode accelerates the reaction kinetics of water electrolysis

Lu Zhan[a, b], Yanru Liu[a, c], Guizhong Zhou[b*], Kang Liu[a, c], Yunmei Du[a, b*], Lei Wang[a, c]

[a] Key Laboratory of Eco-chemical Engineering, Ministry of Education, International Science and Technology Cooperation Base of Eco-chemical Engineering and Green Manufacturing, Qingdao University of Science and Technology, Qingdao, People's Republic of China

[b] Shandong Engineering Research Center for Marine Environment Corrosion and Safety Protection, College of Environment and Safety Engineering, Qingdao University of Science and Technology, Qingdao, People's Republic of China

[c] College of Chemistry and Molecular Engineering, Qingdao University of Science and Technology, Key Laboratory of Optic-electric Sensing and Analytical Chemistry of Life Science, Taishan Scholar Advantage and Characteristic Discipline Team of Eco Chemical Process and Technology, Qingdao, People's Republic of China, Qingdao, People's Republic of China

*E-mail: zhougz@126.com (Guizhong Zhou); duyunmeiqust@163.com

ECSA measurements.

The electrochemically active surface area ECSA can be calculated by the following formula:

$$ECSA=\frac{C_{dl}}{C_s}$$

Among them C_{dl} is the electric double layer capacitance, the unit is mF. And Cs is the constant that converts the capacitance to ECSA, the value is 0.04 mF cm^{-2}. Depending on the electrode material, the specific capacitance of the flat surface is in the range of 20-60 μFcm^{-2}. Here, it is assumed that the calculated value of ECSA is an intermediate value of 40 μF cm^{-2}.

Construction and optimization of Fe_2P/CoP and Ru-Fe_2P/Ru-FeCoP models. Fe_2P/CoP heterojunction modeling uses the CoP (202) crystal plane and Fe_2P (110) crystal plane. CoP and Fe_2P are three layers, in which CoP is a 1*2 expansion cell and Fe_2P is a 1*2 expansion cell. The Ru-Fe_2P/Ru-FeCoP heterojunction ensures that the lattice constants in a direction are consistent, and two Ru atoms are doped at the interface of the heterojunction. At the same time, to avoid the interaction of periodic structures, the vacuum layer is set to 15 A.

Details of DFT calculation.

All the DFT calculations were conducted based on the Vienna Ab-inito Simulation Package (VASP) [S1-S2]. The exchange-correlation effects were described by the Perdew-Burke-Ernzerhof (PBE) functional within the generalized gradient approximation (GGA) method [S3-S4]. The core-valence interactions were accounted by the projected augmented wave (PAW) method [S5]. The energy cutoff for plane wave expansions was set to 400 eV, and the 2×2×1 Monkhorst-Pack grid k-points were selected to sample the Brillouin zone integration. The structural optimization was completed for energy and force convergence set at 1.0×10^{-5} eV and 0.02 eV $Å^{-1}$, respectively. Grimme's DFT-D3 methodology [S6] was used to describe the dispersion interactions.

The Gibbs free energy changes (ΔG) of the reaction are calculated using the following formula:

$$\Delta G = \Delta E + \Delta \mathrm{ZPE} - T\Delta S + \Delta G_{\mathrm{U}} + \Delta G_{\mathrm{pH}}$$

where ΔE is the electronic energy difference directly obtained from DFT calculations, ΔZPE is the zero-point energy difference, T is the room temperature (298.15 K) and

ΔS is the entropy change. $\Delta G_U = -eU$, where U is the applied electrode potential. $\Delta G_{pH} = k_B T \times \ln 10 \times pH$, where k_B is the Boltzmann constant, and pH value is set to 0.

Faraday efficiency calculation (HER and OER):

$$H_2O \rightarrow H_2 + 1/2\ O_2$$

Q=I*t （1）

Q：electric quantity (C)

I：current (A)

t：time (s)

$Q=n*N_0*e*Z$ （2）

Q：electric quantity (C)

n：amount of substance（mol）

N_0：The Avogadro constant is equal to the number of atoms of 1 mol substance.，Its value is about $6.022*10^{23}$（mol^{-1}）

e：The charge of a single electron，$1.602x10^{-19}$（C）

Z：The number of electron transfer of reaction

The charge carried by each mole of electrons is 1, and the Faraday constant F is about 96485 Coulomb（C/mol）. that is :

$F=1*N_0*e$ （3）

Therefore, substituting into Equation (2), the electric quantity Q can be expressed as : Q = n*F*Z (4) For the electrolysis of 1 mol of water to produce 1 mol of hydrogen and 0.5 mol of oxygen :

(Anode) $Q_A=n_A*Z_A*F=0.5\ mol*4*F=2*96485\ C=192970\ C$

(Cathode)$Q_C=n_C*Z_C*F=1\ mol*2*F=2*96485\ C=192970\ C$

Back to (1), 1 Coulomb represents the amount of charge passed by a current of 1 ampere in 1 second :**1C=1A*1s**

Since **192970 C=53.6 A·h**

$FE=n_{ex}/n*100\%=Q_{ex}/Q_{th}*100\%$

Therefore, by substituting the above formula: FE_{HER}=99.8 % FE_{OER}=99.4 %

Activation energy calculation (HER and OER)： The process of obtaining the activation energy value (Ea) is as follows: Firstly, the LSV curves of HER and OER at 25 °C (298K), 35 °C (308K), 45 °C (318K), 55 °C (328K) were measured respectively **(Fig. S17 and S19)**. Then, the extension lines of Tafel slopes at different temperatures are taken. When η=0, the abscissa is $Logj_0$ ($Logj_0$ is negative) **(Fig. S18 and S20).** With $Logj_0$ as the ordinate and 1000/T (K^{-1}) as the abscissa, Arrhenius linear curves of FeCoP/FF-Q, Ru-FeCoP/FF and Ru-FeCoP/FF-C are obtained (**Fig. 4c-d).** The activation energy values (Ea) of FeCoP/FF-Q, Ru-FeCoP/FF and Ru-FeCoP/FF-C were obtained by the activation energy formula $Ea=2.3*R*[d(logj_0)/d(T^{-1})]$.

HER:

Ru-FeCoP/FF: $Ea_1=2.3*R*[d(logj_0)/d(T^{-1})]=2.3*8.32*1.71=32.7$ KJ mol^{-1}

FeCoP/FF-Q：$Ea_2=2.3*R*[d(logj_0)/d(T^{-1})]=2.3*8.32*2.77=53.1$ KJ mol-1

Ru-FeCoP/FF-C：$Ea_3=2.3*R*[d(logj_0)/d(T^{-1})]=2.3*8.32*2.1=40.2$ KJ mol^{-1}

OER:

Ru-FeCoP/FF: $Ea_1=2.3*R*[d(logj_0)/d(T^{-1})]=2.3*8.32*1.87=35.8$ KJ mol^{-1}

FeCoP/FF-Q：$Ea_2=2.3*R*[d(logj_0)/d(T^{-1})]=2.3*8.32*3.7=70.8$ KJ mol-1

Ru-FeCoP/FF-C：$Ea_3=2.3*R*[d(logj_0)/d(T^{-1})]=2.3*8.32*2.25=43.1$ KJ mol^{-1}

Supplementary Figures and Tables

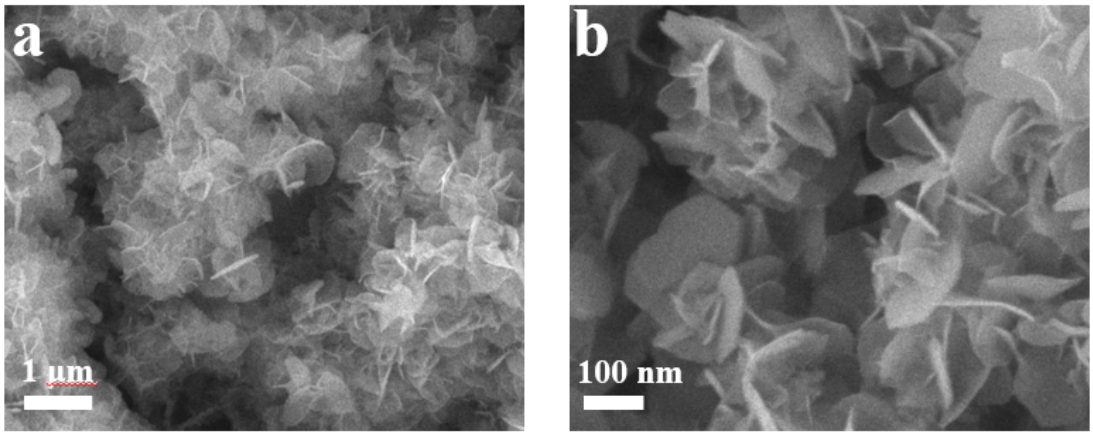

Fig. S1 SEM images of $CoFe_2O_4$/FF.

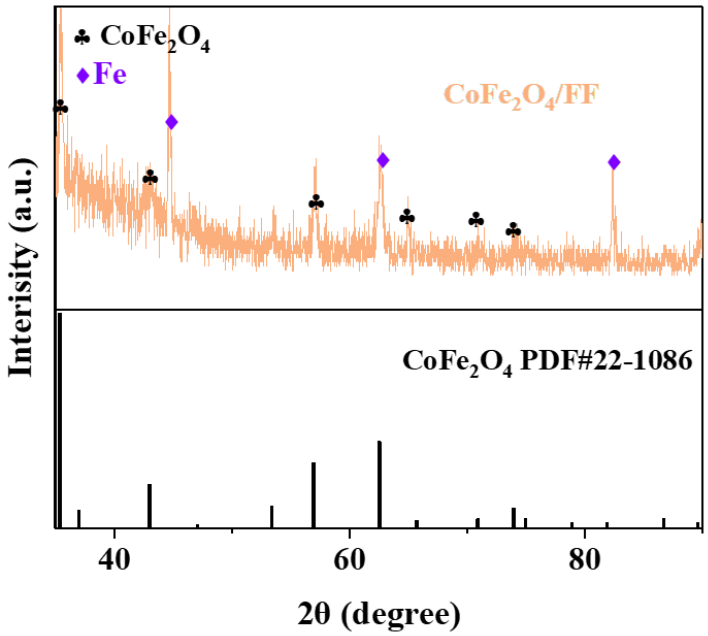

Fig. S2 XRD patterns $CoFe_2O_4$/FF electrode

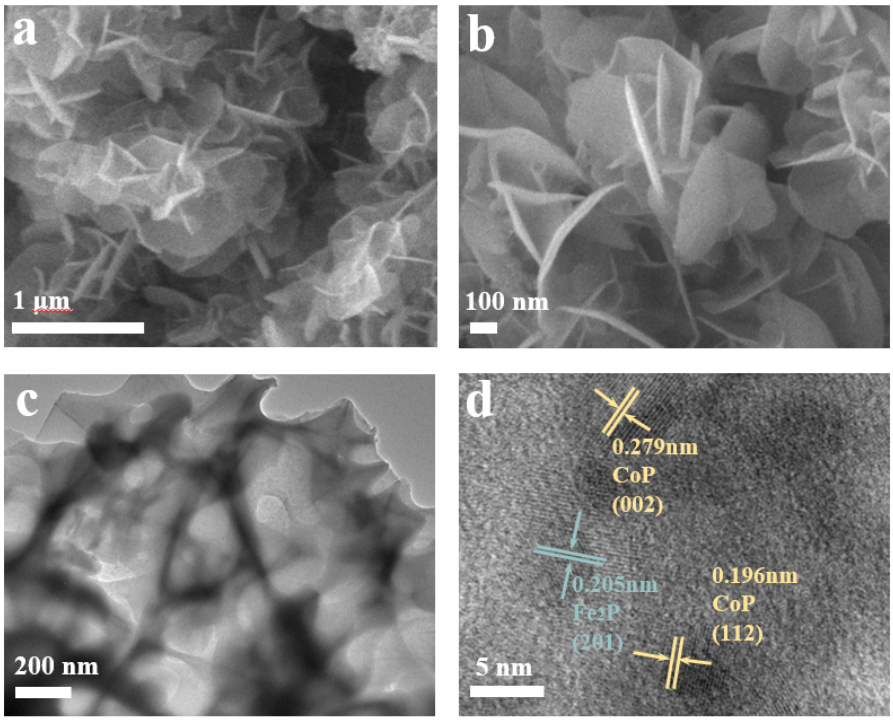

Fig. S3 (a-b) SEM images of FeCoP/FF-Q. (c) TEM image of powders on the surface of FeCoP/FF-Q electrode. (d) HRTEM images of powders on the surface of FeCoP/FF-Q electrode

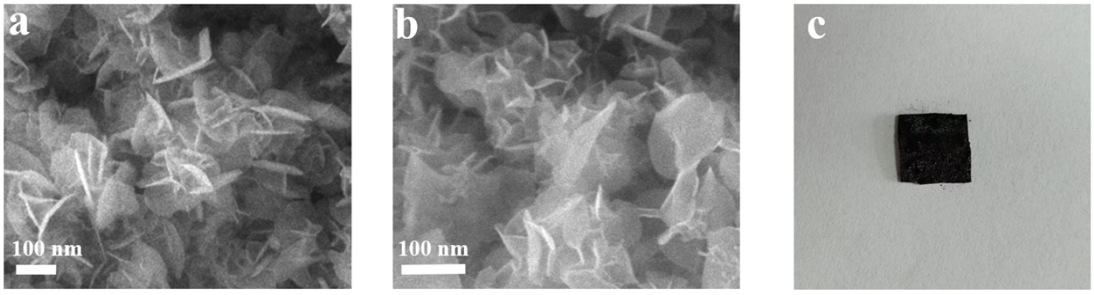

Fig. S4 (a-b) SEM images of FeCoP/FF-C and (c) digital image of Ru-FeCoP/FF catalyst.

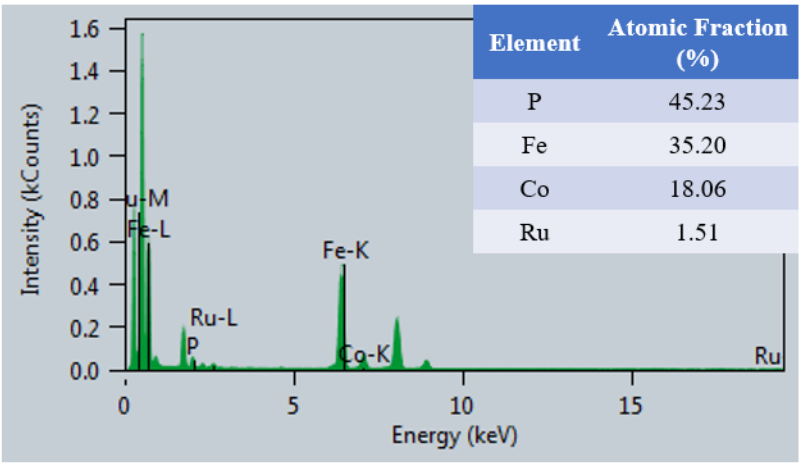

Element	Atomic Fraction (%)
P	45.23
Fe	35.20
Co	18.06
Ru	1.51

Fig. S5 EDS spectrum of Ru-FeCoP/FF

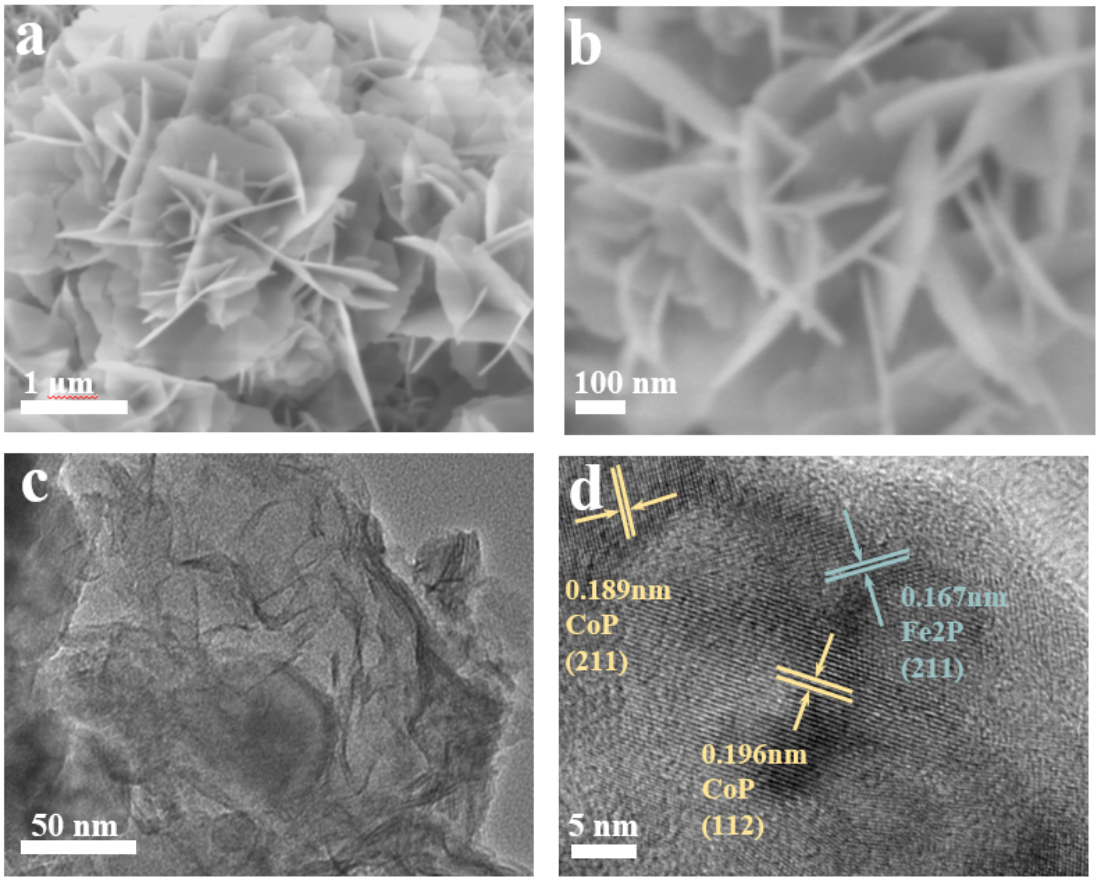

Fig. S6 (a-b) SEM images of Ru-FeCoP/FF-C. (c) TEM image of surface powder on Ru-FeCoP/FF-C electrode. (d) HRTEM images of surface powder on Ru-FeCoP/FF-C electrode.

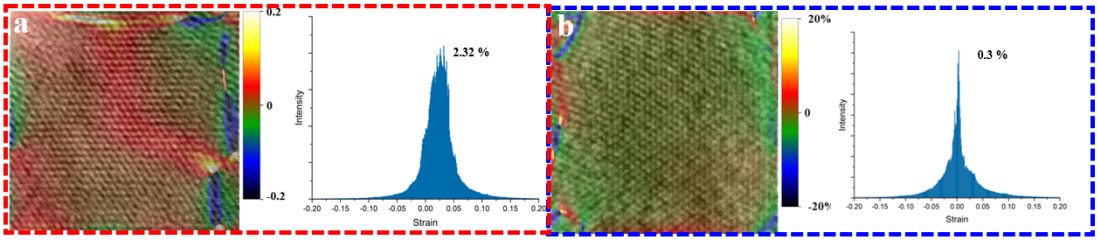

Fig. S7 (a-b) GPA (Geometric phase analysis) test of Ru-FeCoP/FF and Ru-FeCoP/FF-C electrode

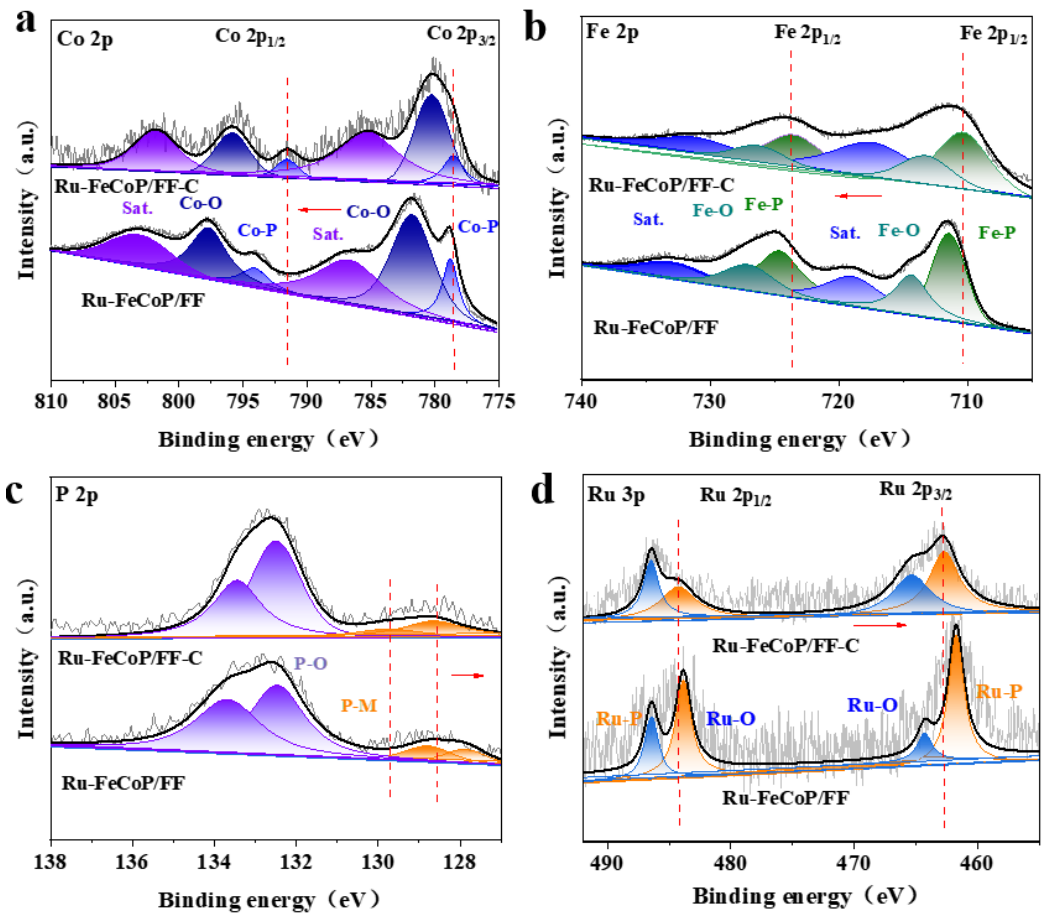

Fig. S8 (a-b) High-resolution spectra of (c) Co 2p (d) Fe 2p (e) P 2p (f) Ru 3p of Ru-FeCoP/FF and Ru-FeCoP/FF-C electrode

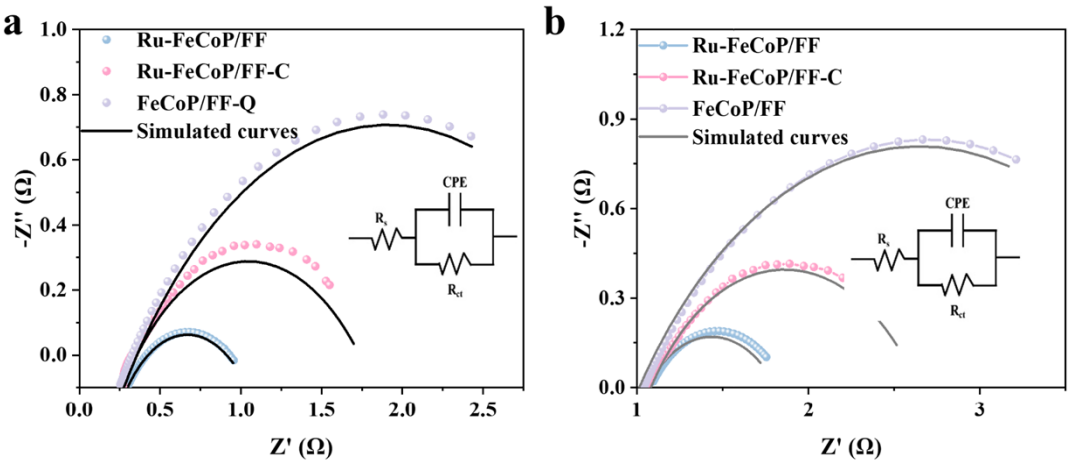

Fig. S9 Nyquist plots of Ru-FeCoP/FF, Ru-FeCoP/FF-C, FeCoP/FF-Q for HER and OER.

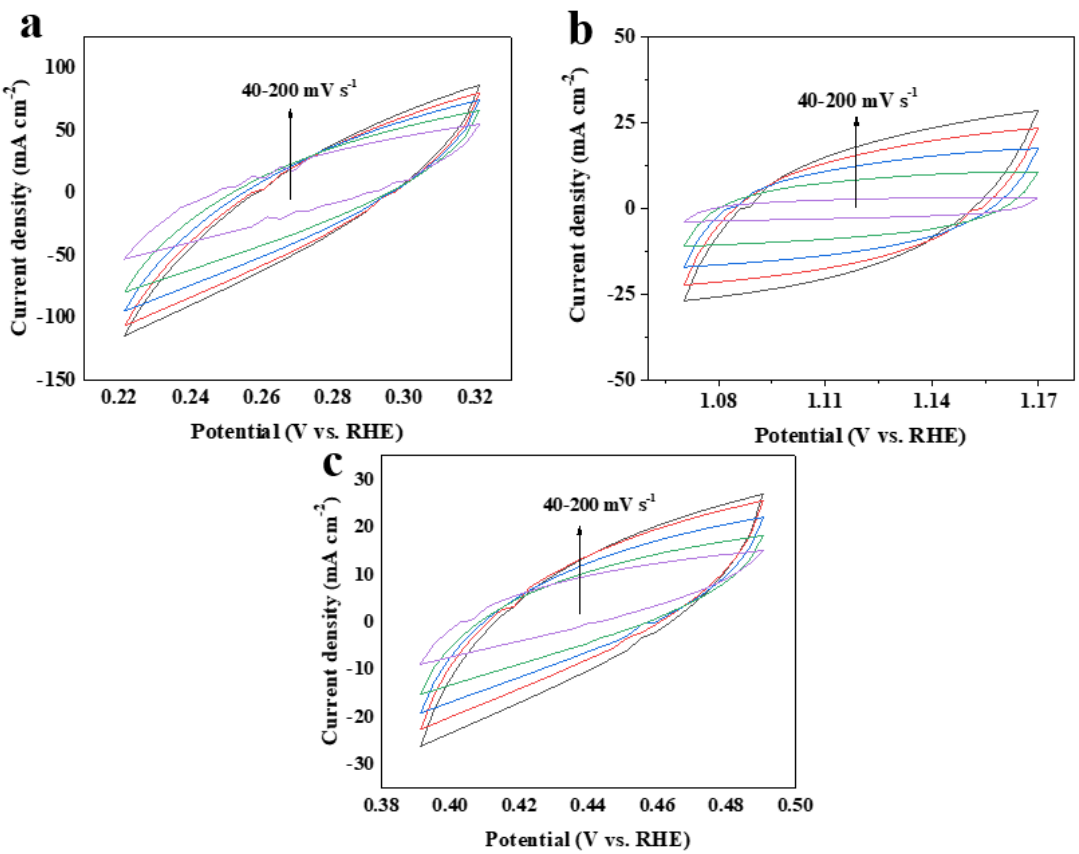

Fig. S10 CVs curves at different scan rates from 40 to 200 mV s^{-1} of HER in 1.0M KOH. (a) Ru-FeCoP/FF. (b) Ru-FeCoP/FF-C. (c) FeCoP/FF-Q

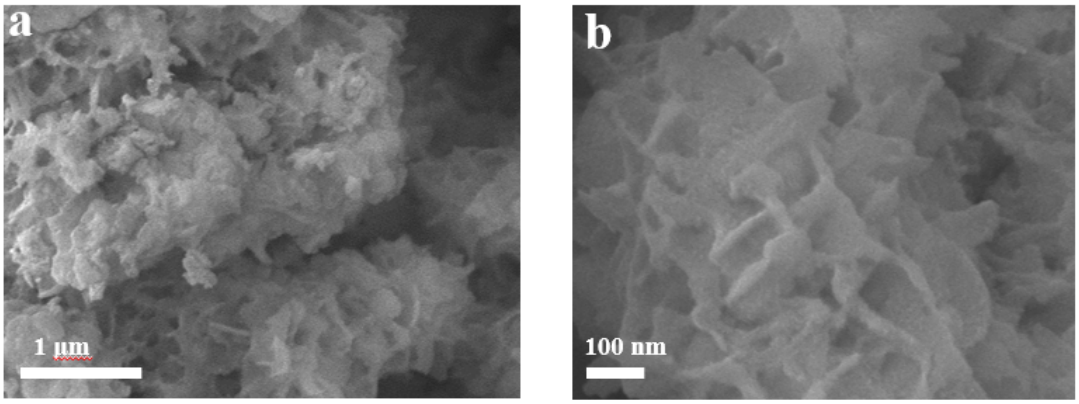

Fig. S11 SEM images of Ru-FeCoP/FF after HER

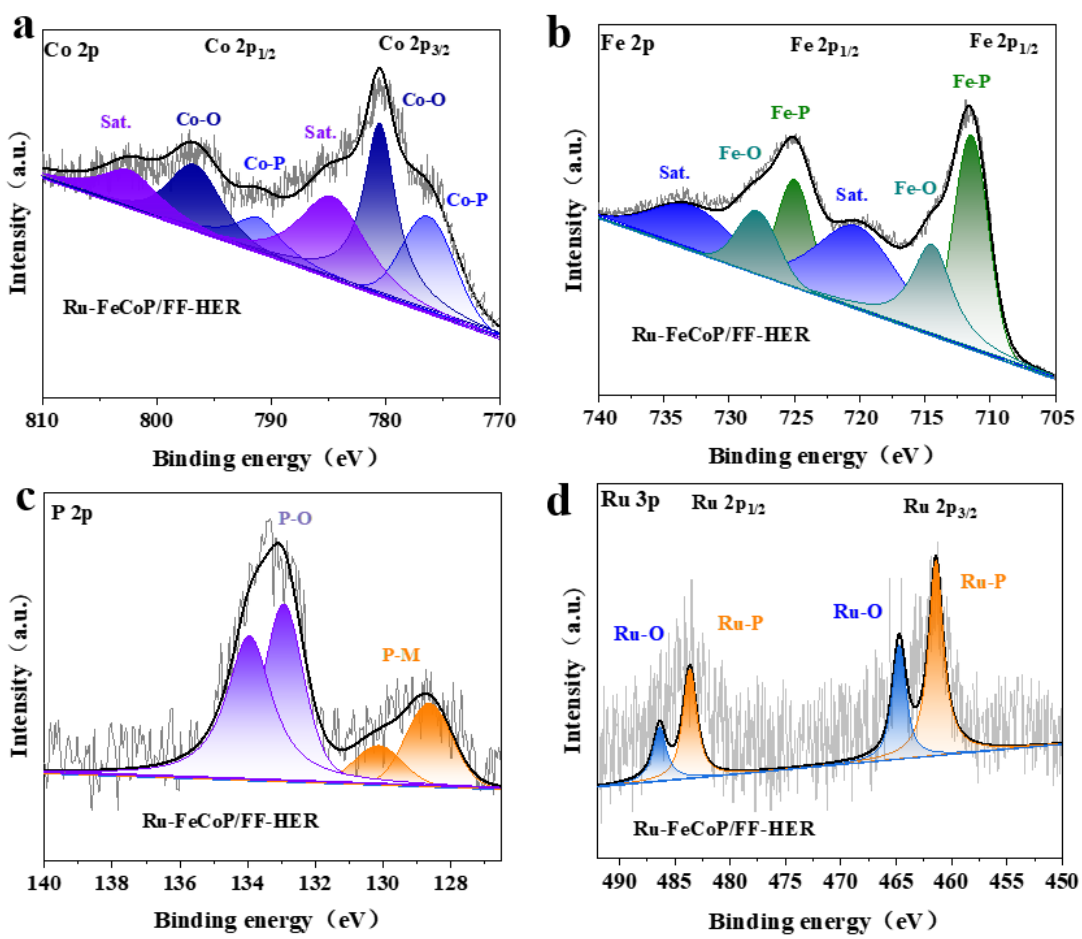

Fig. S12 High-resolution spectra of (c) Co 2p (d) Fe 2p (e) P 3p (f) Ru 3p of Ru-FeCoP/FF electrode after HER

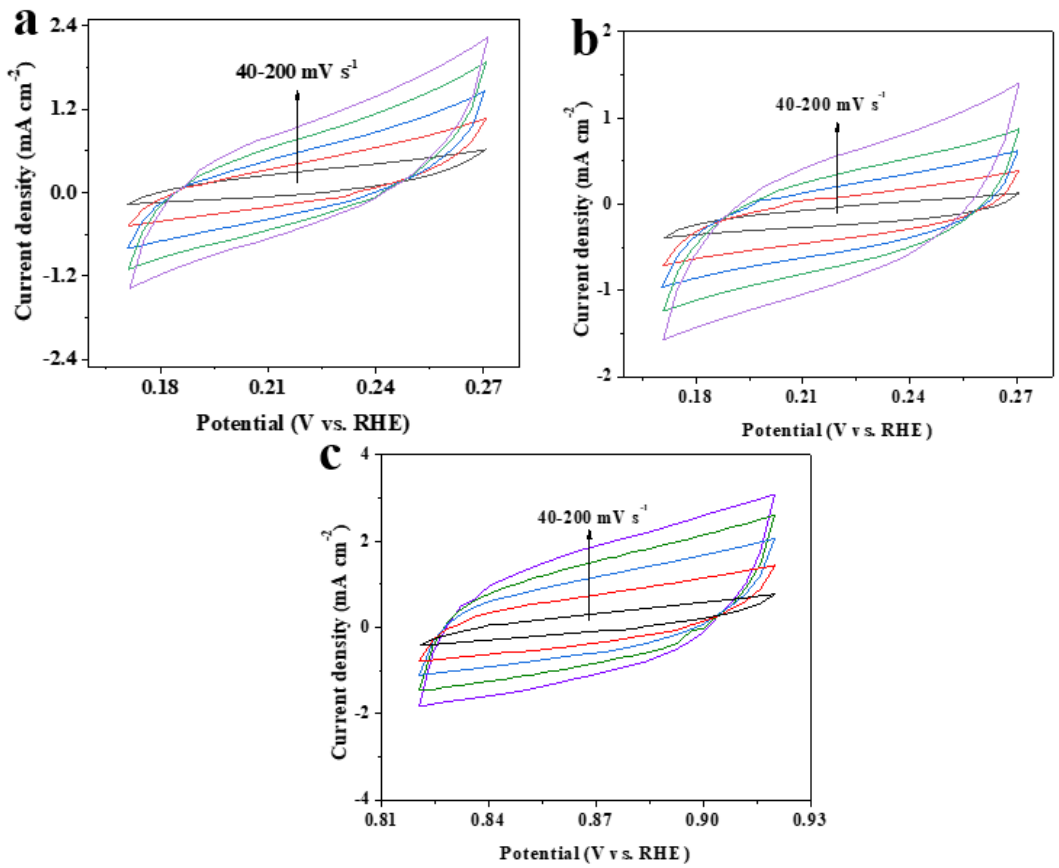

Fig. S13 CVs curves at different scan rates from 40 to 200 mV s-1 of OER in 1.0M KOH. (a) Ru-FeCoP/FF. (b) Ru-FeCoP/FF-C. (c) FeCoP/FF-Q

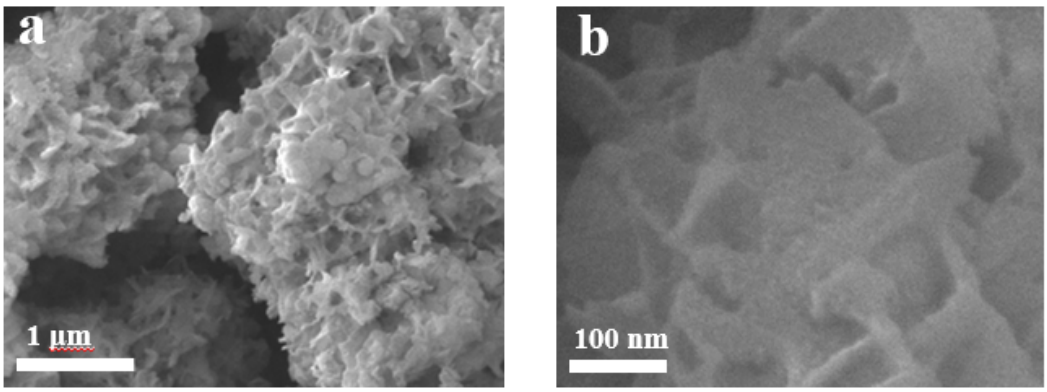

Fig. S14 (a-b) SEM images of Ru-FeCoP/FF after OER

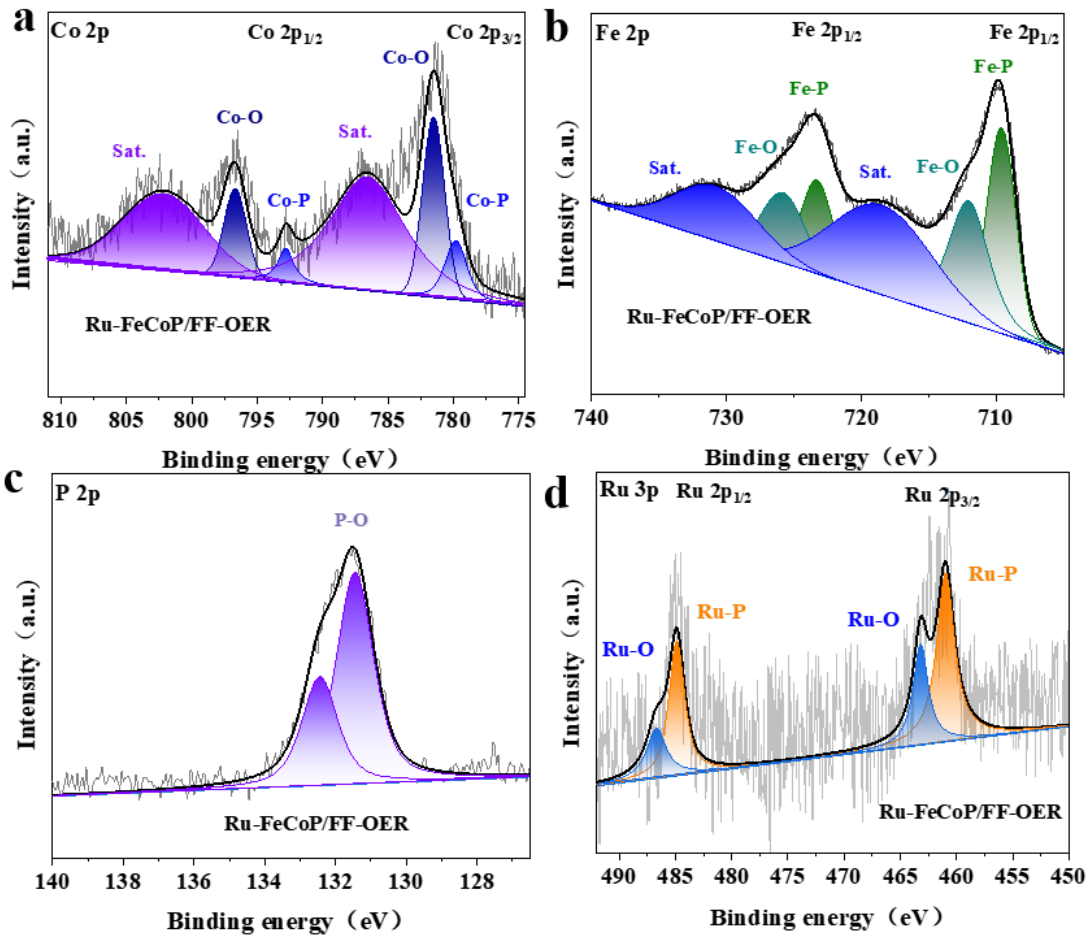

Fig. S15 High-resolution spectra of (c) Co 2p (d) Fe 2p (e) P 3p (f) Ru 3p of Ru-FeCoP/FF electrode after OER

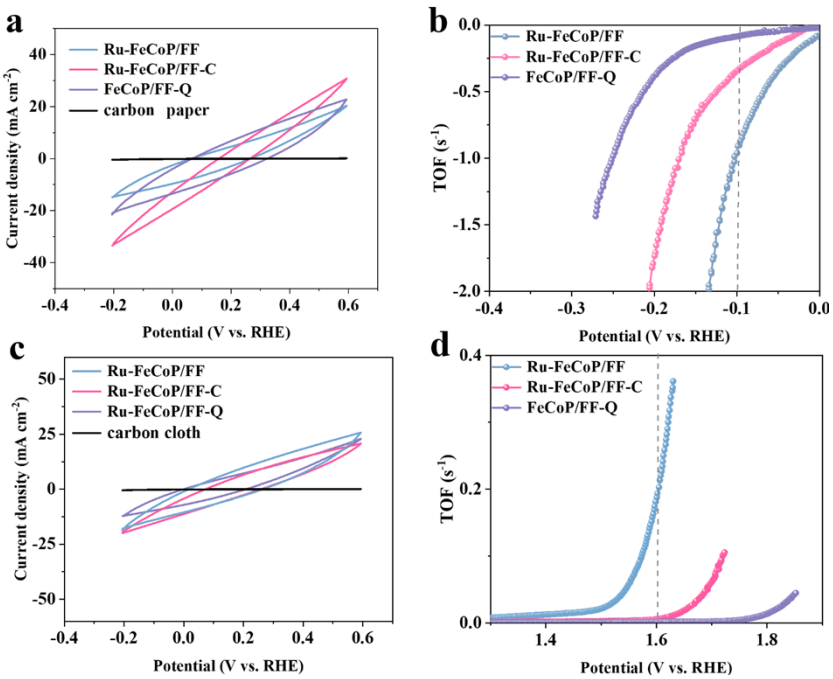

Fig. S16 (a-c) Cyclic Voltammograms of Ru-FeCoP/FF, Ru-FeCoP/FF-C, FeCoP/FF-Q in 1.0 M PBS at scanning rate of 100 mV s^{-1} for HER (b-d) Calculated turnover frequencies (TOFs) at various voltages for HER of Ru-FeCoP/FF, Ru-FeCoP/FF-C, FeCoP/FF-Q

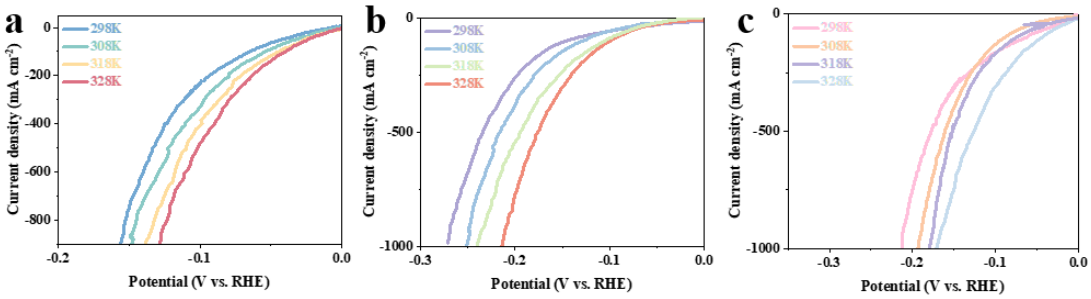

Fig. S17 LSV curves of the (a) Ru-FeCoP/FF; (b) FeCoP/FF-Q; (c) Ru-FeCoP/FF-C catalysts at 298~328 K for HER

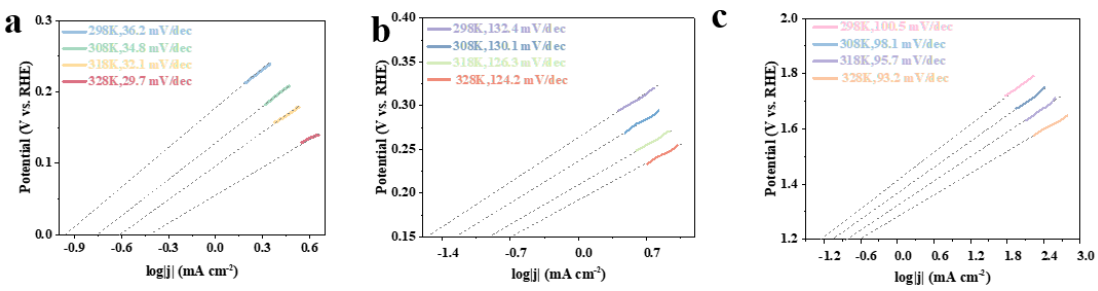

Fig. S18 exchange current density curves of the the (a) Ru-FeCoP/FF; (b) FeCoP/FF-Q; (c) Ru-FeCoP/FF-C catalysts at 298~328 K for HER

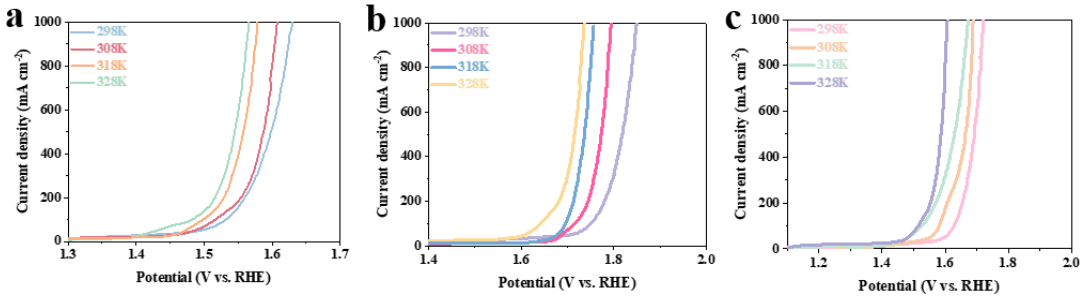

Fig. S19 LSV curves of the (a) Ru-FeCoP/FF; (b) FeCoP/FF-Q; (c) Ru-FeCoP/FF-C catalysts at 298~328 K for OER

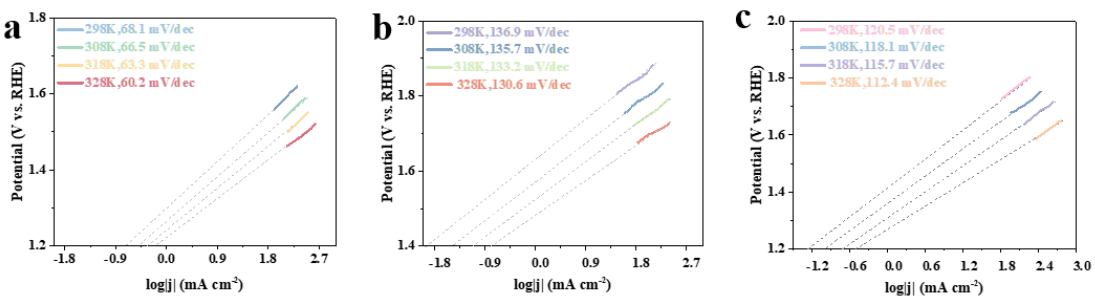

Fig. S20 exchange current density curves of the the (a) Ru-FeCoP/FF; (b) FeCoP/FF-Q; (c) Ru-FeCoP/FF-C catalysts at 298~328 K for OER

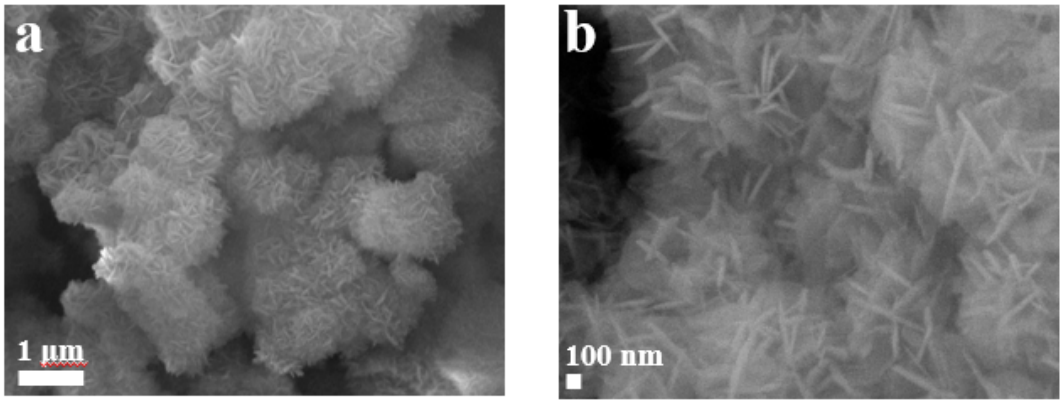

Fig. S21 (a-b)SEM images of Ru-FeCoP/FF-20

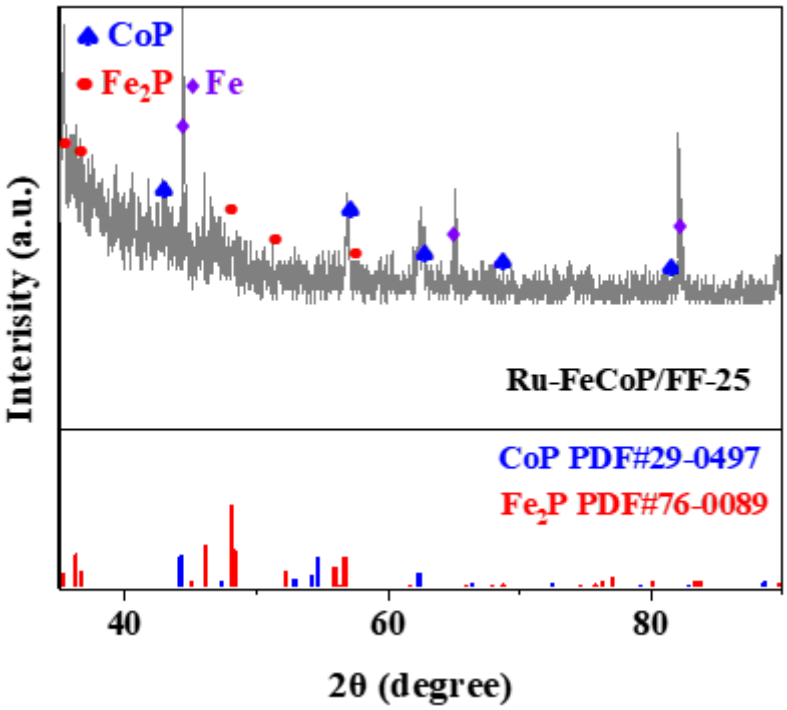

Fig. S22 XRD patterns of Ru-FeCoP/FF-20 electrode

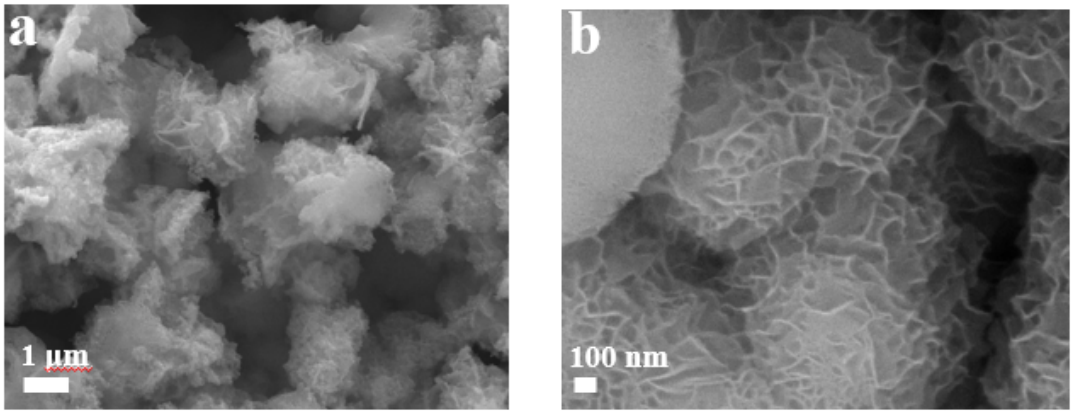

Fig. S23 (a-b) SEM images of Ru-FeCoP/FF-25

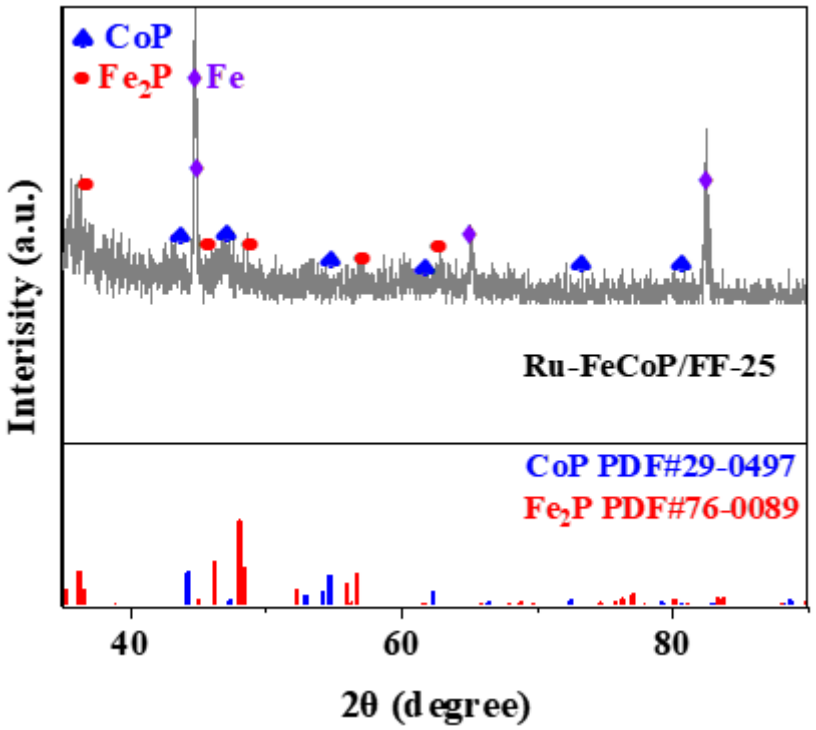

Fig. S24 XRD patterns of Ru-FeCoP/FF-25 electrode

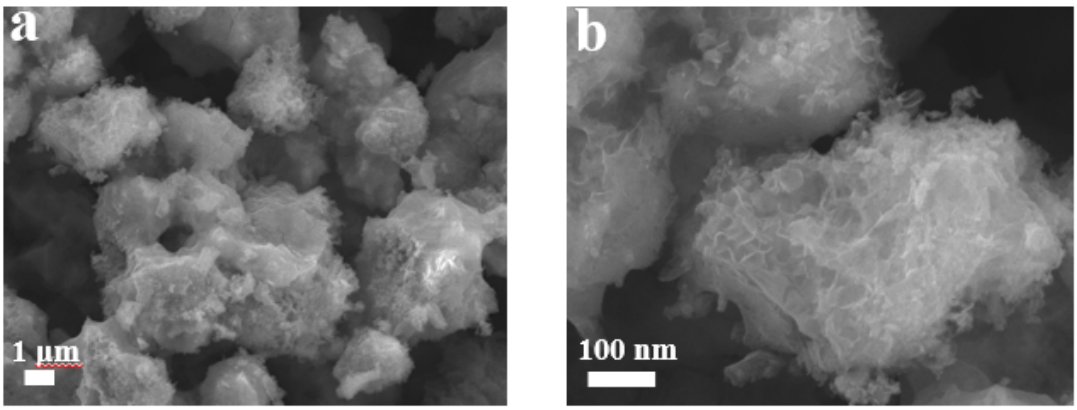

Fig. S25 (a-b) SEM images of Ru-FeCoP/FF-35

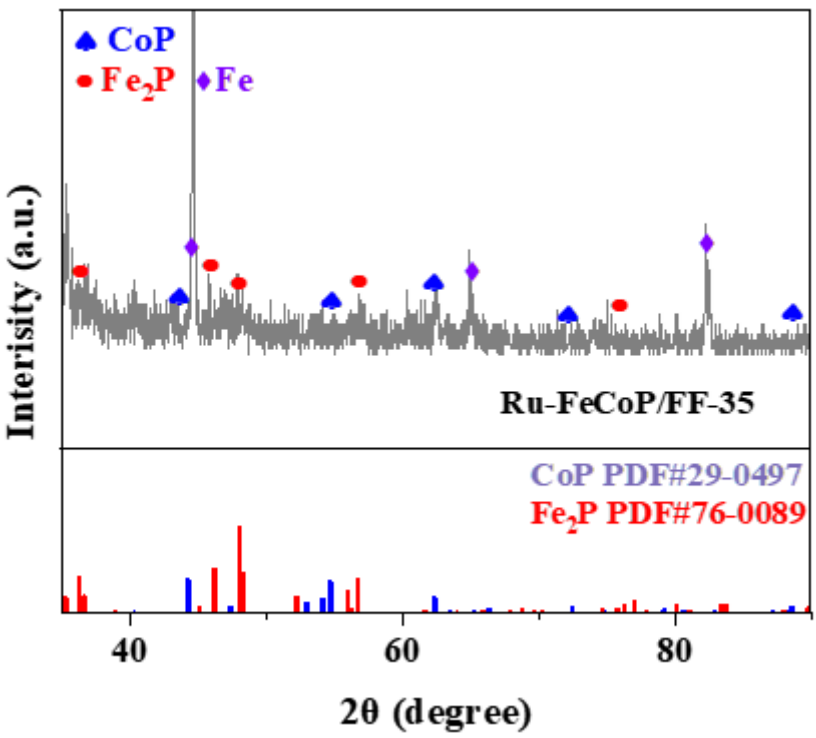

Fig. S26 XRD patterns of Ru-FeCoP/FF-35 electrode

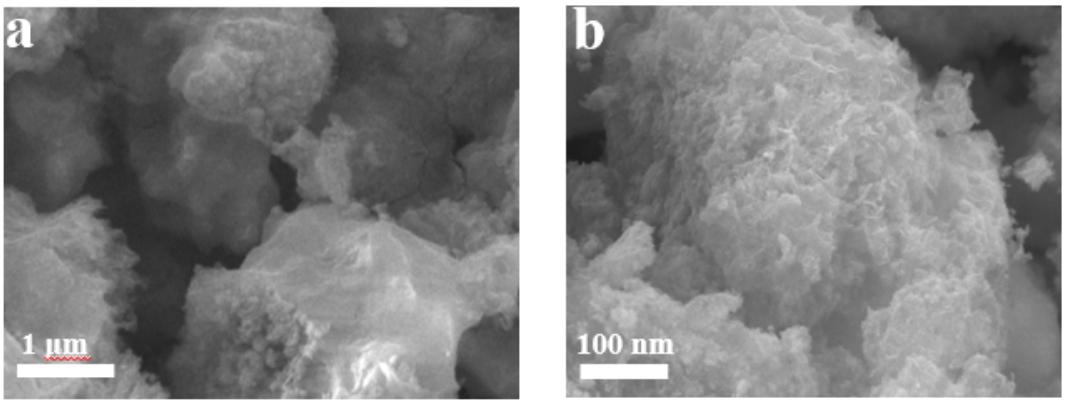

Fig. S27 (a-b) SEM images of Ru-FeCoP/FF-40

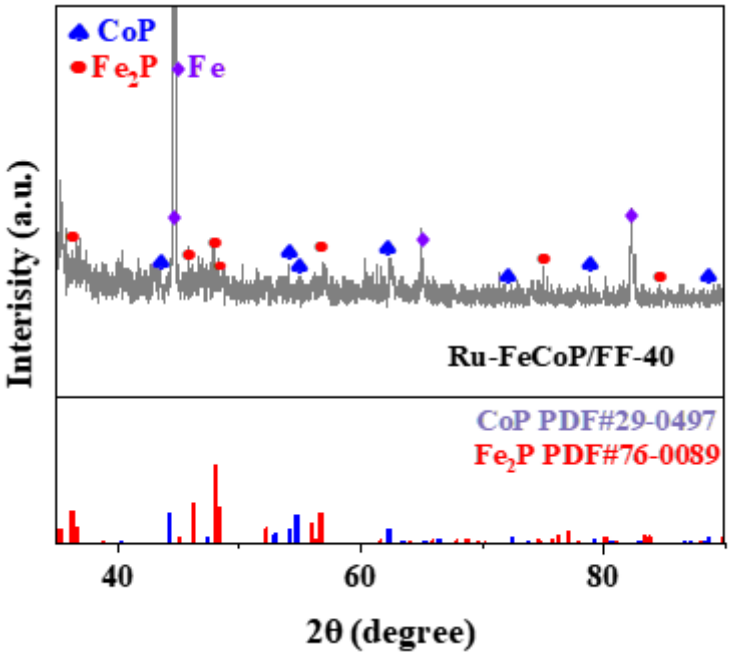

Fig. S28 XRD patterns of Ru-FeCoP/FF-40 electrode

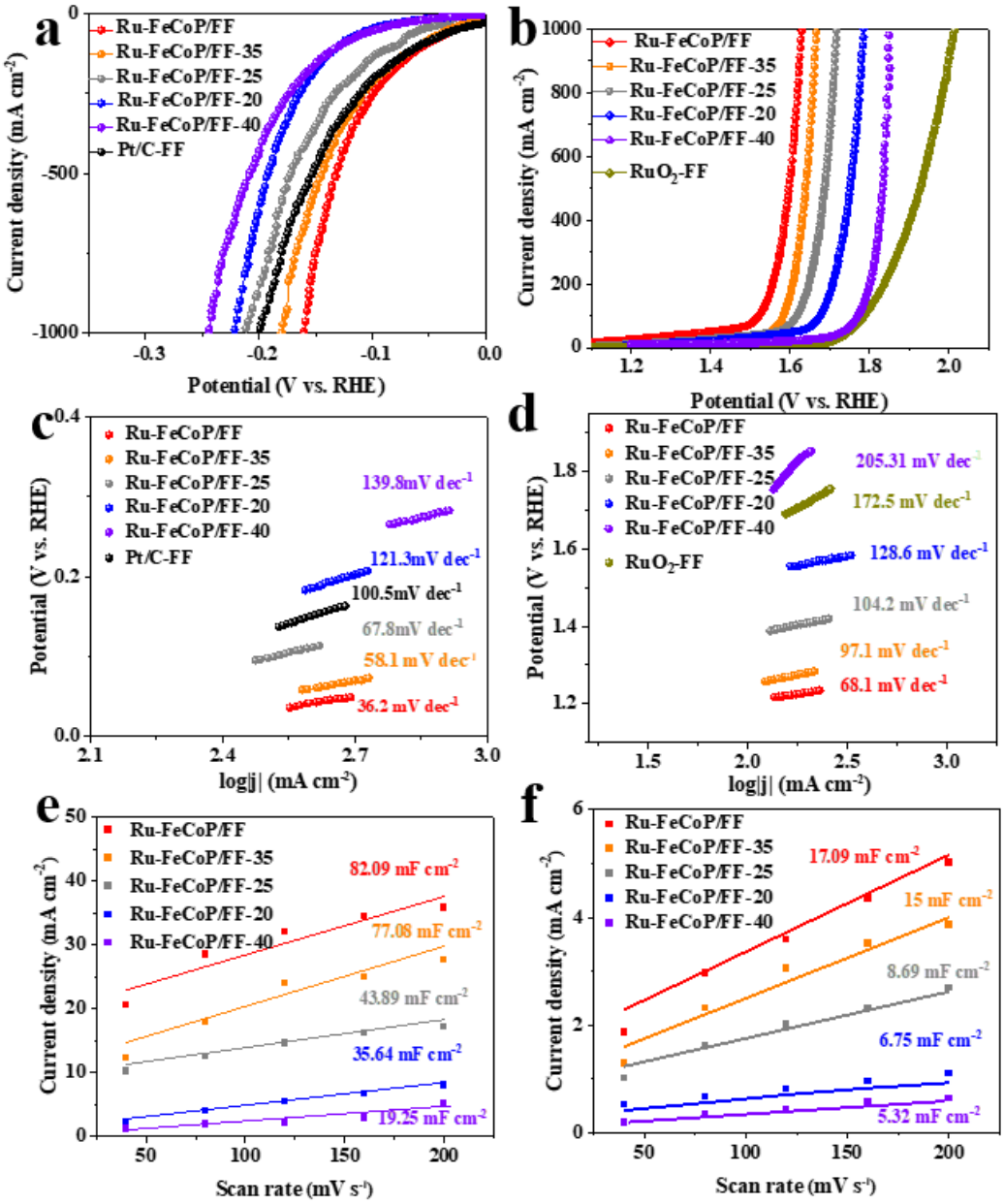

Fig. S29 HER and OER performance in 1.0 M KOH. (a-b) Polarization curves of Ru-FeCoP/FF, Ru-FeCoP/FF-35, Ru-FeCoP/FF-25, Ru-FeCoP/FF-20, Ru-FeCoP/FF-40 and Pt/C-FF(Ru-FeCoP/FF, Ru-FeCoP/FF-35, Ru-FeCoP/FF-25, Ru-FeCoP/FF-20,Ru-FeCoP/FF-40 and RuO_2-FF) with iR-compensation, (c-d) Corresponding Tafel plots of Ru-FeCoP/FF(Ru-FeCoP/FF), Ru-FeCoP/FF-35(Ru-FeCoP/FF-35) Ru-FeCoP/FF-25(Ru-FeCoP/FF-25), Ru-FeCoP/FF-20(Ru-FeCoP/FF-20) , Ru-FeCoP/FF-40(Ru-FeCoP/FF-40) and Pt/C-FF(RuO_2-FF) (e-f) C_{dl} measurements of Ru-FeCoP/FF(Ru-FeCoP/FF), Ru-FeCoP/FF-35(Ru-FeCoP/FF-35) Ru-FeCoP/FF-25(Ru-FeCoP/FF-25), Ru-FeCoP/FF-20(Ru-FeCoP/FF-20), Ru-FeCoP/FF-40(Ru-FeCoP/FF-40) for HER and OER

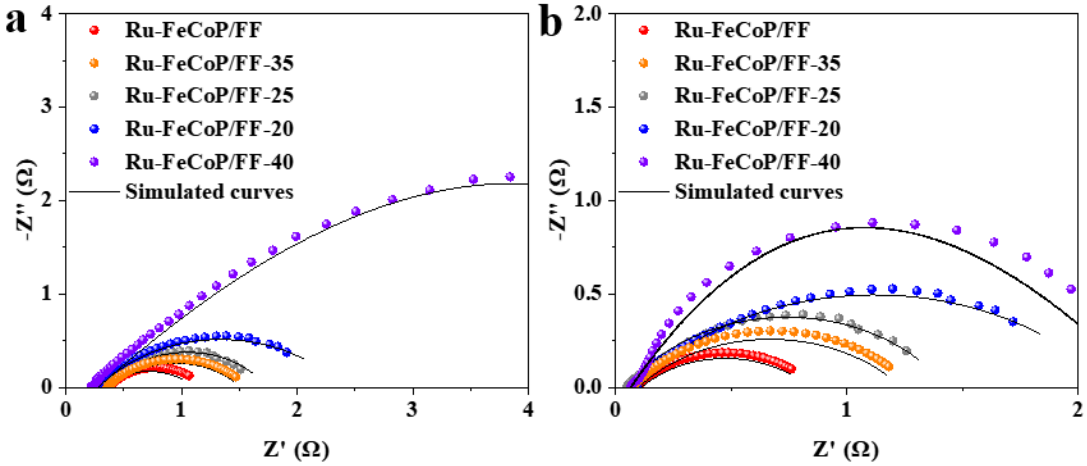

Fig. S30 (a-b) Nyquist plots of Ru-FeCoP/FF(Ru-FeCoP/FF), Ru-FeCoP/FF-35(Ru-FeCoP/FF-35) Ru-FeCoP/FF-25(Ru-FeCoP/FF-25), Ru-FeCoP/FF-20(Ru-FeCoP/FF-20 , Ru-FeCoP/FF-40(Ru-FeCoP/FF-40 for HER and OER.

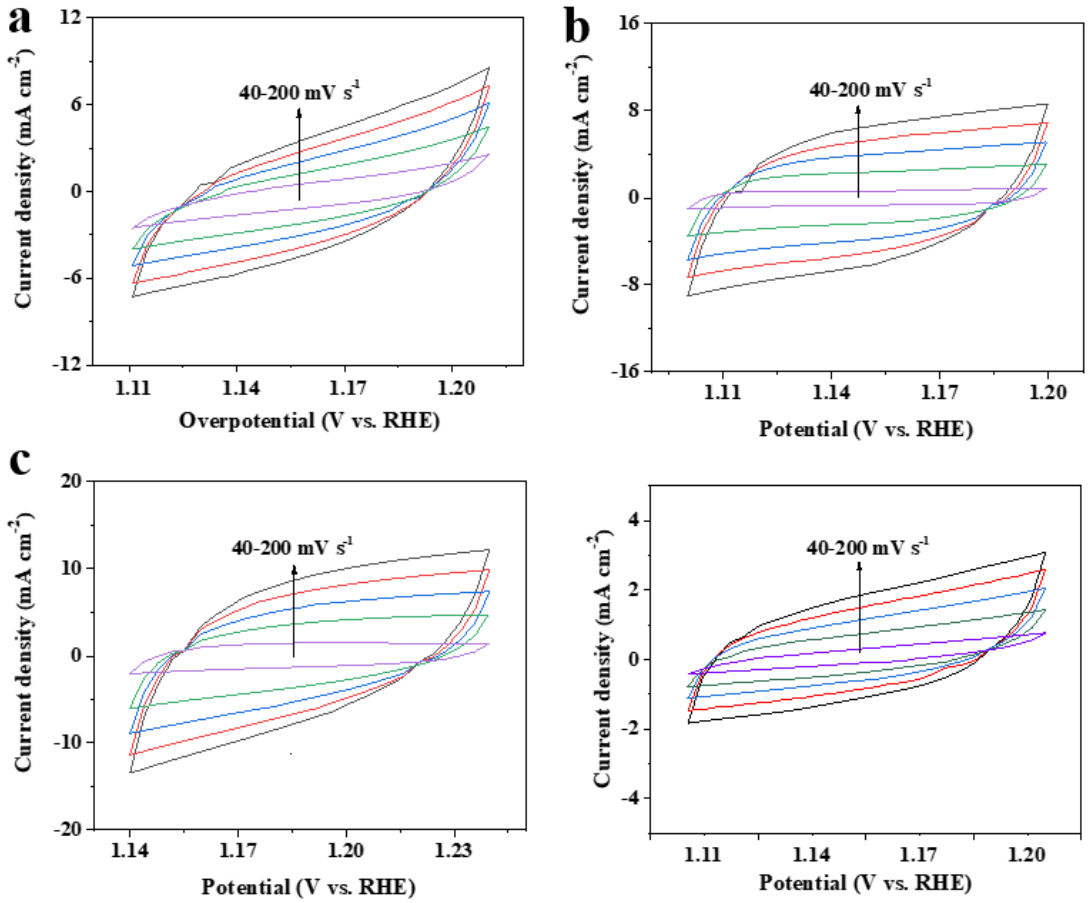

Fig. S31 CVs curves at different scan rates from 40 to 200 mV s^{-1} of HER in 1.0M KOH. (a) Ru-FeCoP/FF-20. (b) Ru-FeCoP/FF-25. (c) Ru-FeCoP/FF-35. (d) Ru-FeCoP/FF-40

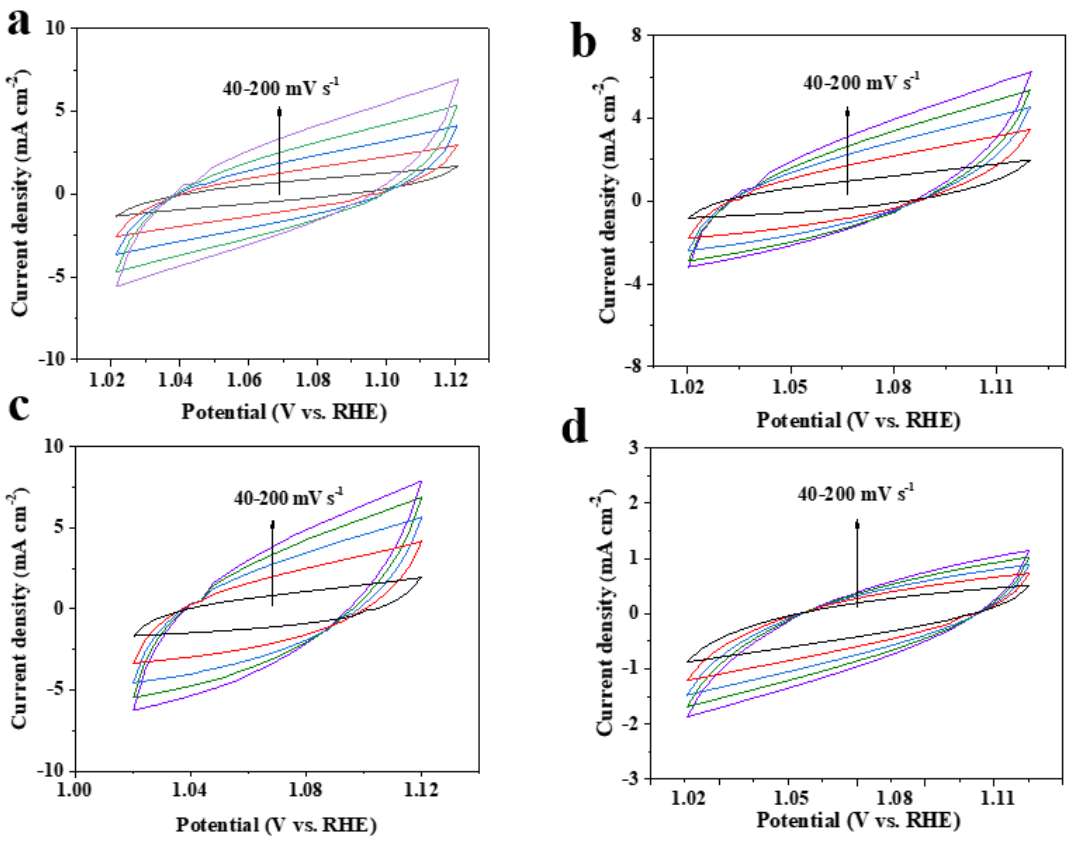

Fig. S32 CVs curves at different scan rates from 40 to 200 mV s^{-1} of OER in 1.0M KOH. (a) Ru-FeCoP/FF-20. (b) Ru-FeCoP/FF-25. (c) Ru-FeCoP/FF-35. (d) Ru-FeCoP/FF-40

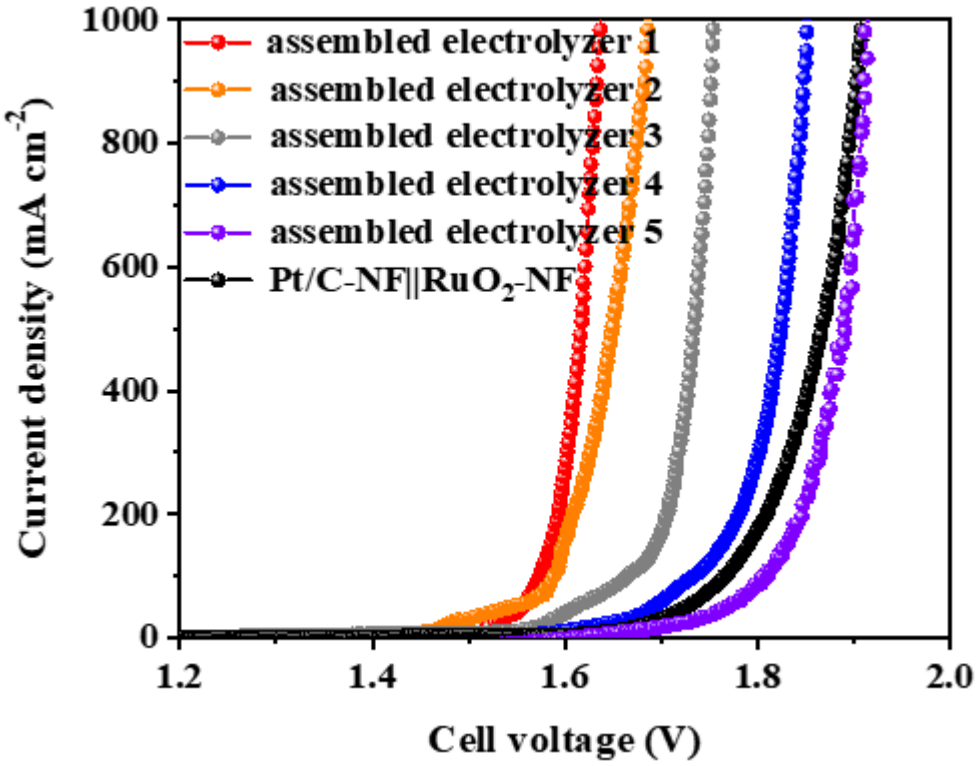

Fig S33 Overall water splitting tests in 1.0 M KOH. LSV of Ru-FeCoP/FF||Ru-FeCoP/FF (assembled electrolyzer 1), Ru-FeCoP/FF-35||Ru-FeCoP/FF-35 (assembled electrolyzer 2), Ru-FeCoP/FF-25||Ru-FeCoP/FF-25 (assembled electrolyzer 3), Ru-FeCoP/FF-20||Ru-FeCoP/FF-20 (assembled electrolyzer 4), Ru-FeCoP/FF-40||Ru-FeCoP/FF-40 (assembled electrolyzer 5) and Pt/C-FF||RuO_2-FF

Table S1 ICP content table of surface powder on electrode Ru-FeCoP/FF, Ru-FeCoP/FF-20, 25, 35, 40 and Ru-FeCoP/FF-C electrode

ICP Content	Ru (wt %)
ICP Content	Ru (wt %)
Ru-FeCoP/FF	1.82
Ru-FeCoP/FF-20	1.04
Ru-FeCoP/FF-25	1.54
Ru-FeCoP/FF-35	2.56
Ru-FeCoP/FF-40	3.17
Ru-FeCoP/FF-C	0.51

Table S2. The fitted R_{ct} value of Ru-FeCoP/FF, Ru-FeCoP/FF-C and FeCoP/FF-Q catalyst for HER and OER.

Electrocatalysts	R_{ct} for HER (Ω)	R_{ct} for OER (Ω)
Ru-FeCoP/FF	0.74	0.69
Ru-FeCoP/FF-C	1.44	1.52
FeCoP/FF-Q	2.17	2.33

Table S3. The fitted R_{ct} value of Ru-FeCoP/FF catalyst and other comparative samples for HER and OER.

Electrocatalysts	R_{ct} for HER (Ω)	R_{ct} for OER (Ω)
Ru-FeCoP/FF	0.74	0.69
Ru-FeCoP/FF-35	1.18	1.07
Ru-FeCoP/FF-25	1.36	1.29
Ru-FeCoP/FF-20	2.08	1.89
Ru-FeCoP/FF-40	4.68	2.11

Table S4. ECSA table of Ru-FeCoP/FF, Ru-FeCoP/FF-C, FeCoP/FF-Q for HER

Electrocatalysts	C_{dl} (mF cm^{-2})	C_{DL} (mF)	ECSA (cm^2)
Ru-FeCoP/FF	82.09	328.36	8209
Ru-FeCoP/FF-C	47.68	190.72	4768
FeCoP/FF-Q	23.6	94.4	2360

Table S5. ECSA table of Ru-FeCoP/FF, Ru-FeCoP/FF-C, FeCoP/FF-Q for OER

Electrocatalysts	C_{dl} (mF cm^{-2})	C_{DL} (mF)	ECSA (cm^2)
Ru-FeCoP/FF	17.09	68.36	1709
Ru-FeCoP/FF-C	7.75	31	775
FeCoP/FF-Q	2.05	8.2	205

Table S6. The overpotential required for a noble metal-based electrocatalyst in an alkaline environment at 100 mA cm^{-2} has recently been reported for overall water splitting.

Electrocatalysts	j (mA cm^{-2})	η (V)	References
Ru-FeCoP/FF	100	1.54	This Work
$Ni_{12}P_5$–Fe_2P–NbP	100	1.65	S7
CoNi/$CoFe_2O_4$/NF	100	1.75	S8
Ru-MoS_2-Mo_2C/TiN	100	1.7	S9
MoO_2-$MoNi_4$	100	1.61	S10
H-NMO/CMO/CF-450	100	1.71	S11
CoNi/$CoFe_2O_4$/NF	100	1.75	S12
Ru, Ni–CoP	100	1.60	S13
HP-Ru/C	100	1.61	S14
Ru-CMOP	100	1.697	S15
Ru/Co–N–C-800°C	100	1.7	S16
Ni_3S_2-NiFe LDHs/NF	100	1.71	S17
S-FeNiOOH	100	1.81	S18
MnCoP/NF	100	1.97	S19
Ni_2P-Ru_2P/NF	100	2	S20
Ru-MoS_2-Mo_2C/TiN	100	2.2	S21

References

[S1] G. Kresse, J. Hafner, Ab Initiomolecular Dynamics for Liquid Metals, Phys. Rev. B, 1993, 47, 558-561.

[S2] G. Kresse, J. Hafner, Ab Initiomolecular-Dynamics Simulation of the Liquid-Metal-Amorphous-Semiconductor Transition in Germanium, Phys. Rev. B, 1994, 49, 14251-14269.

[S3] J. P. Perdew, K. Burke, M. Ernzerhof, Generalized Gradient Approximation Made Simple. Phys. Rev. Lett., 1996, 77, 3865-3868.

[S4] G. Kresse, D. Joubert, From Ultrasoft Pseudopotentials to the Projector Augmented-Wave Method. Phys. Rev. B, 1999, 59, 1758-1775.

[S5] P. E. Blöchl, Projector Augmented-Wave Method, Phys. Rev. B, 1994, 50, 17953-17979.

[S6] Grimme, S.; Antony, J.; Ehrlich, S.; Krieg, H. J. Chem. Phys., 2010, 132, 154104.

[S7] X. Mu, X. Gu , S. Dai, J. Chen, Y. Cui, Q. Chen, M. Yu, C. Chen, S. Liu, S. Mu, Breaking the symmetry of single-atom catalysts enables an extremely low energy barrier and high stability for large-current-density water splitting, Energy Environ. Sci., 2022, 15, 4048-4057.

[S8] P. Zhai, P. Xia, M. Wu, Y. Zhang, G. Gao, J. Zhang, B. Cao, S. Zhang, Y. Li, Z. Fan, Z. Wang, C. Zhang, X. J. T. Miller, L. Sun, J. Hou, Engineering single-atomic ruthenium catalytic sites on defective nickel-iron layered double hydroxide for overall water splitting, Nat. Commun., 2021, 12, 4587.

[S9] H. Su, S. Song, Y. Gao, N. Li, Y. Fu, L. Ge, W. Song, J. Liu, T. Ma, In Situ

Electronic Redistribution Tuning of $NiCo_2S_4$ Nanosheets for Enhanced Electrocatalysis, Adv. Funct. Mater., 2022, 32, 210973.

[S10] H. Zhang, C. Chen, X. Wu, C. Lv, Y. Lv, J. Guo, D. Jia, Synergistic Incorporating RuO_2 and NiFeOOH Layers onto Ni_3S_2 Nanoflakes with Modulated Electron Structure for Efficient Water Splitting. Small Methods., 2022, 6, 2200483.

[S11] H. Zhang, A. Aierke, Y. Zhou, Y. Ni, L. Feng, A. Chen, T. Wågberg, G. Hu, A high-performance transition-metal phosphide electrocatalyst for converting solar energy into hydrogen at 19.6% STH efficiency, Carbon Energy, 2022, 5, e217

[S12] Q. Gao, W. Luo, X. Ma, Z. Ma, S. Li, F. Gou, W. Shen, Y. Jiang, R. He, M. Li, Electronic modulation and vacancy engineering of Ni9S8 to synergistically boost efficient water splitting: Active vacancy-metal pairs. Appl. Catal. B 2022, 310, 121356

[S13] Y. Song, J. Cheng, J. Liu, Q. Ye, X. Gao, J. Lu, Y. Cheng, Modulating electronic structure of cobalt phosphide porous nanofiber by ruthenium a nd nickel dual doping for highly-efficiency overall water splitting at high current density, Appl. Catal. B, 2021, 298.

[S14] S. Wang, B. Xu, W. Huo, H. Feng, X. Zhou, F. Fang, Z. Xie, J. K. Shang, J. Jiang, Efficient FeCoNiCuPd thin-film electrocatalyst for alkaline oxygen and hydrogen evolution reactions. Appl. Catal. B, 2022, 313.

[S15] Q. Quan, Y. Zhang, F. Wang, X. Bu, W. Wang, Y. Meng, P. Xie, D. Chen, W. Wang, D. Li, C. Liu, S. Yip, J. C. Ho, Topochemical domain engineering to construct 2D mosaic heterostructure with internal electric field for high-performance overall

water splitting, Nano Energy, 2022, 101, 1075.

[S16] V. H. Hoa, D. T. Tran, S. Prabhakaran, D. H. Kim, N. Hameed, H. Wang, N. H. Kim, J. H. Lee, Ruthenium single atoms implanted continuous MoS_2-Mo_2C heterostructure for high-performance and stable water splitting, Nano Energy, 2021, 88, 10627.

[S17] S. W. Wu, S. Q. Liu, X. H. Tan, W. Y. Zhang, K. Cadien, Z. Li, Ni_3S_2-embedded NiFe LDH porous nanosheets with abundant heterointerfaces for high-current water electrolysis. Chem. Eng. J., 2022, 442, 13610.

[S18] S. Yan, W. Liao, M. Zhong, W. Li; C. Wang, N. Pinna, W. Chen, X. Lu, Partially oxidized ruthenium aerogel as highly active bifunctional electrocatalyst for overall water splitting in both alkaline and acidic media, Appl. Catal. B, 2022, 307, 121199.

[S19] S. Yang, J. Y. Zhu, X. N. Chen, M. J. Huang, S. H. Cai, J. Y. Han, J. S. Li, Self-supported bimetallic phosphides with artificial heterointerfaces for enhanced electrochemical water splitting, Appl. Catal. B, 2022, 304, 120914.

[S20] V. H. Hoa, D. T. Tran, S. Prabhakaran, D. H. Kim, N. Hameed, H. Wang, N. H. Kim, J. H. Lee, Ruthenium single atoms implanted continuous MoS_2-Mo_2C heterostructure for high-performance and stable water splitting, Nano Energy, 2021, 88, 10627.